LANGMUIR

pubs.acs.org/Langmuir Article

Gold Nanocluster Extracellular Vesicle Supraparticles: Self-Assembled Nanostructures for Three-Dimensional Uptake Visualization

Ulrike Kauscher,[#] Jelle Penders,[#] Anika Nagelkerke, Margaret N. Holme, Valeria Nele, Lucia Massi, Sahana Gopal, Thomas E. Whittaker, and Molly M. Stevens*

Cite This: *Langmuir* 2020, 36, 3912−3923

Read Online

ACCESS | Metrics & More | Article Recommendations | Supporting Information

ABSTRACT: Extracellular vesicles (EVs) are secreted by the vast majority of cells and are being intensively studied due to their emerging involvement in a variety of cellular communication processes. However, the study of their cellular uptake and fate has been hampered by difficulty in imaging EVs against the cellular background. Here, we show that EVs combined with hydrophobic gold nanoclusters (AuNCs) can self-assemble into supraparticles, offering an excellent labeling strategy for high-resolution electron microscopic imaging in vitro. We have tracked and visualized the reuptake of breast cancer cell-derived EV AuNC supraparticles into their parent cells, from early endocytosis to lysosomal degradation, using focused ion beam-scanning electron microscopy (FIB-SEM). The presence of gold within the EVs and lysosomes was confirmed via DF-STEM EDX analysis of lift-out sections. The demonstrated formation of AuNC EV supraparticles will facilitate future applications in EV imaging as well as the EV-assisted cellular delivery of AuNCs.

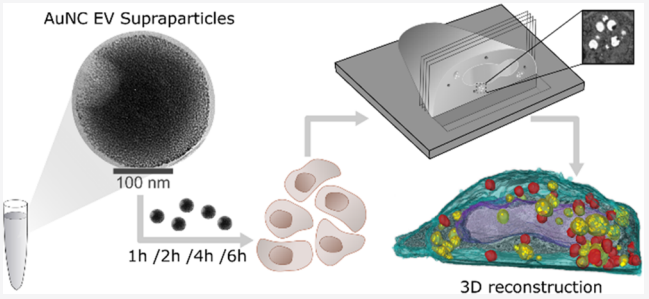

INTRODUCTION

Extracellular vesicles (EVs) are important cell-to-cell communication vehicles common to both eukaryotic and prokaryotic cells.[1−3] They are 30−1000-nm diameter phospholipid bilayer vesicles, the lumen of which contains proteins, nucleic acids, metabolites, and other molecules derived from the parental cell cytosol,[4−7] and the membrane itself contains a diverse population of lipids and proteins.[8]

These biological nanoparticles are able to transport biomolecules between cells over large intercellular distances[9−11] and therefore have considerable potential for therapeutic and diagnostic purposes.

EVs are being studied extensively as potential biocompatible drug delivery vehicles due to their intrinsic nontoxicity and stability in vivo and are readily taken up by cells. EVs can be loaded with hydrophilic, hydrophobic, or amphiphilic drugs[12] using a range of techniques including electroporation, saponin treatment, and hypotonic dialysis.[13] As such, EVs have been used for in vivo drug delivery within multiple disease settings,[12] including the delivery of anti-inflammatory drugs,[14,15] short interfering RNA for Alzheimer's therapy,[16,17] chemotherapeutic drugs, and photosensitizers.[18−20] In addition to their use as drug delivery vehicles, the intrinsic biology of EVs is of great interest, especially with regard to their roles in cancer and metastasis. It has been shown that cancer cells secrete large numbers of EVs,[21,22] and cancer-derived EVs have been implicated in the development of the metastatic niche.[23,24] It is therefore of great interest to find new ways of investigating EV−cell interactions in greater detail.

Although gold nanoparticles are a well-established tool in nanotechnology, utilized in many ways in recent decades,[25] small gold nanoclusters (AuNCs) have only recently emerged as a distinct novel material with extremely promising properties.[26] AuNCs have a diameter of <3 nm and consist of a limited number of gold atoms that are stabilized by ligands. The atomic packing, electronic structure, magnetism, electrochemical, and charge transport properties of AuNCs differ vastly from those of larger gold nanoparticles. AuNCs have unique photochemical characteristics due to the molecule-like properties obtained by the quantization of their conduction band.[27] This makes them a powerful tool in diagnostic applications. In addition to being traceable using a variety of imaging modes, they also have therapeutic potential due to their photothermal properties.[28,29] Under carefully controlled conditions, these nanoparticles can self-assemble to form larger defined structures, which are termed supraparticles.[30−33]

Received: November 7, 2019
Revised: March 3, 2020
Published: April 6, 2020

https://dx.doi.org/10.1021/acs.langmuir.9b03479
Langmuir 2020, 36, 3912−3923

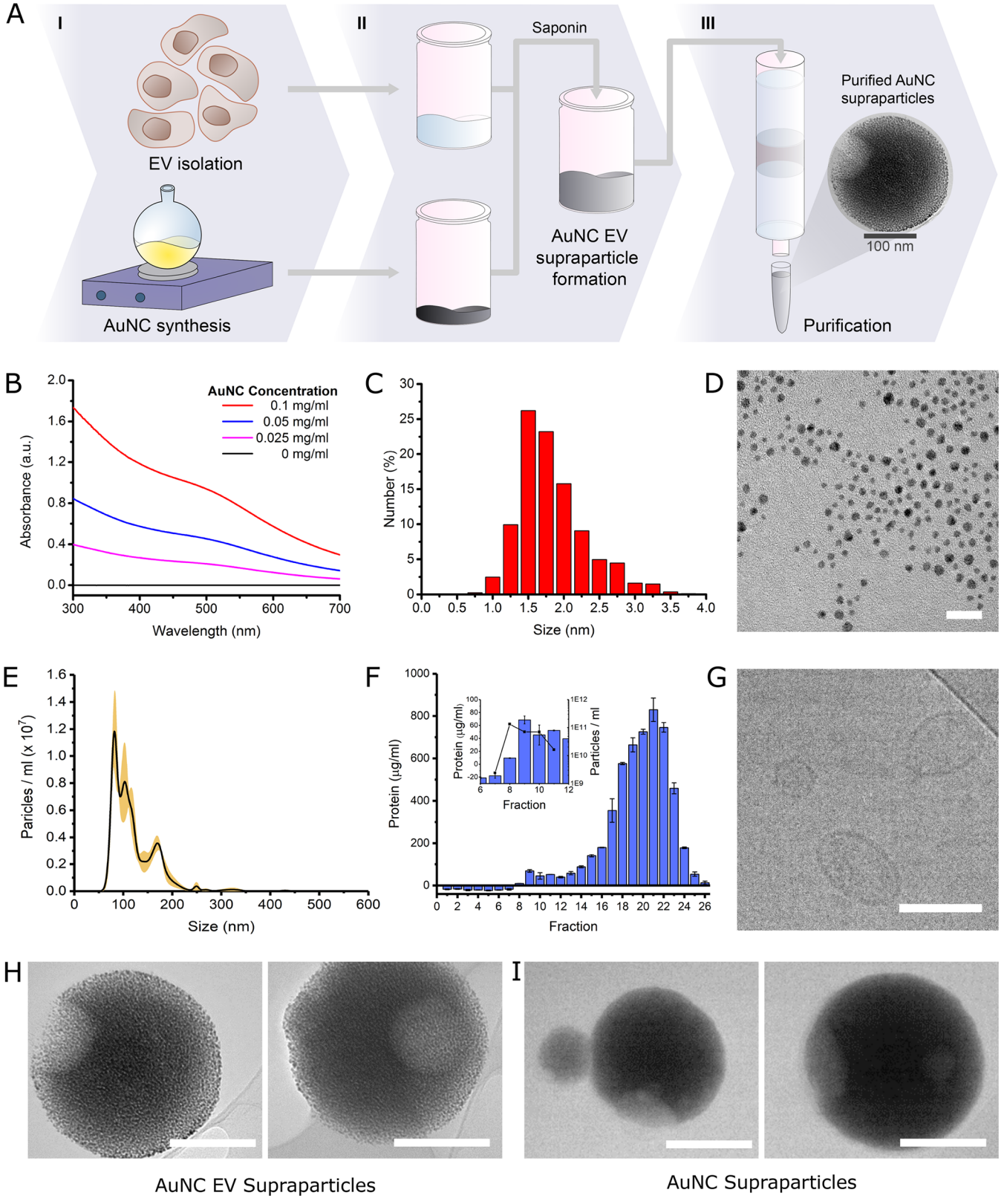

Figure 1. Formation and characterization of AuNC EV supraparticles. (A) AuNC EV supraparticles are formed by the saponin-assisted self-assembly of hydrophobic alkyl-capped AuNCs of around 2 nm in diameter and MDA-MB-231 breast cancer cell-derived EVs and purified using size exclusion chromatography. (B) UV−vis spectroscopy of [AuNC] = 0.0−0.1 mg/mL in $CHCl_3$. (C) Size distribution histogram based on TEM imaging, 1.7 ± 0.5 nm (mean ± s.d., n = 805). (D) TEM representative micrograph of AuNCs, scale bar 10 nm. (E) NTA analysis of native MDA-MB-231 EVs (mean ± s.e.) 1000-fold diluted in PBS, n = 3. (F) BCA protein quantification of size exclusion chromatography fractions and NTA particle analysis of EV fractions, n = 2. (G−I) Cryo-TEM representative micrographs of (G) native EVs, (H) AuNC EV supraparticles, and (I) AuNC supraparticles, scale bars = 100 nm.

https://dx.doi.org/10.1021/acs.langmuir.9b03479
Langmuir 2020, 36, 3912−3923

Advances in the synthesis of supraparticles have been achieved by the careful choice of building blocks, enabling the tuning of the size, morphology, and functionality of the supraparticles, which has given rise to applications in medicine and biology.[34,35]

Here, we report on the self-assembly of hydrophobic gold nanoclusters (AuNCs) and extracellular vesicles (EVs) into supraparticles (Figure 1A). Furthermore, we investigate the toxicity of the supraparticles and their reuptake into the EV parental breast cancer cell line and compare the properties of AuNC supraparticles assembled with or without EVs. Using focused ion beam-scanning electron microscopy (FIB-SEM), we created detailed 3D reconstructions of cells to directly visualize the intracellular uptake and distribution of the self-assembled biomaterial. With FIB-SEM, slices of resin-embedded cells can be cut down to 5−10 nm thickness and imaged sequentially in situ. The resulting image stack can be aligned, and following manual segmentation, a detailed 3D model of the subcellular structure is obtained.[36,37] To the best of our knowledge, this is the first study on the formation of these highly complex self-assembled AuNC EV supraparticles and the first in-depth study and 3D visualization of EV uptake into cells via FIB-SEM. In this study, we pioneer a general route of engineering EVs with nanoparticles, designed to provide insight into how EVs can influence the uptake mechanism of nanoparticles. The self-assembled AuNC EV supraparticles demonstrate a way to bring together the best of two worlds: the biocompatibility of EVs and the versatility of metal nanoparticles. While outside the scope of this study, the proposed method should be easily adaptable to a wide range of small hydrophobic nanoparticles, paving the way for a versatile approach of engineering metal nanoparticle functionalities into biocompatible EVs.

RESULTS AND DISCUSSION

Gold Nanoclusters (AuNCs). These were synthesized via the adaptation of a kinetically controlled two-phase method by Zhu et al. at around 4 °C,[38] here aimed at synthesizing particles <5 nm in diameter, rather than one atomically precise cluster size, to enable incorporation in a phospholipid bilayer membrane. In short, gold(III) salts were reduced via the addition of an octanethiol to an intermediate Au(I)-SR complex and further reduced to Au(0) by strong reducing agent $NaBH_4$. The particles were analyzed via UV−vis spectroscopy and TEM as seen in Figure 1B−D. The spectra obtained via UV−vis spectroscopy do not show any distinctive plasmon resonance signals, indicating that the particles are small AuNCs predominantly less than 3 nm in size. Further analysis of the particles was carried out via transmission electron microscopy (TEM). Small spherical particles were observed with a size of 1.7 ± 0.5 nm (mean ± s.d., n = 805). We were able to consistently achieve clusters within our reported size range, over multiple separate syntheses.

Extracellular Vesicles (EVs). These were isolated from an adenocarcinoma breast epithelial cell line (MDA-MB-231). Cells were cultured for 48 h under serum-free conditions to prevent contamination with serum vesicles. The conditioned medium was harvested from the cells and then concentrated via spin filtration and purified via size exclusion chromatography (SEC). The obtained vesicles were analyzed with BCA protein quantification assays, nanoparticle tracking analysis (NTA), and cryo-TEM (Figure 1E,F). The BCA quantification assay was carried out on each 1 mL fraction of the 24 mL of eluent after SEC (Figure 1F).

The column trace shows a smaller peak for fractions 6−12 and a larger one for fractions 16−24. The EVs are eluted in fractions 6−12 and the signal is due to EV proteins, while the larger signal at fractions 16−24 originates from soluble extracellular proteins not associated with EVs.

Cryo-TEM images of fractions 6−12 show spherical particles with a membrane thickness of 5 nm and a diameter in the range of 30 to 500 nm (Figure 1G). The size range is confirmed by the NTA measurements (Figure 1D). The large polydispersity is characteristic for EVs, as they consist of a heterogenic population of exosomes (approximately 30−100 nm) and microvesicles (up to 1000 nm). Due to the overlap of size and marker proteins, separation of the two populations is not readily achievable.

AuNC EV Supraparticle Formation and Analysis. AuNC EV supraparticles were prepared and analyzed as a new self-assembled hybrid between an inorganic material (AuNCs) and a natural building block (EVs) via a saponin-assisted encapsulation procedure (Figure 1A). Saponin is a plant-derived amphiphilic glycoside that self-assembles with cholesterol in bilayer membranes and can permeabilize membrane bilayers. Saponin has previously been used to permeabilize EVs for the loading of small molecules in drug delivery applications.[13] The use of saponin is advantageous over other methods such as electroporation as it does not alter the size distribution or zeta potential. Here, the addition of saponin and AuNCs to a solution of EVs resulted in supraparticles—large self-assembled entities consisting of small particles and EVs in the size regime of the parent EVs.

The challenge of creating supraparticles lies in overcoming the repulsive forces between the nanoparticles, which has been previously achieved by diverse methods.[30] Surfactant-based procedures are commonly used to form supraparticles in aqueous environments, and the surfactant concentration and type can even be used to affect the supraparticle structure.[39] This is the first time that AuNCs have been combined with EVs to form supraparticles as well as the first use of saponin for supraparticle formation.

After the assembly process, AuNC EV supraparticles were purified using a size exclusion chromatography column. The purification can be observed by the naked eye as the supraparticles run down the column as a gray band (Supporting Information Figure 1A). The whole batch of self-assembled supraparticles, identified by its characteristic color, was collected. After the addition of 500 μL of sample solution to the column, roughly 1 mL of eluate was collected, resulting in an approximate 2-fold dilution.

Supraparticles can also be formed without EVs, by self-assembly of the AuNCs in the presence of saponin. The so-formed EV-free AuNC supraparticles are employed as a control system to monitor the difference in supraparticle−cell interaction behavior with and without the EV building block. However, these AuNC supraparticles proved to be quite unstable, and successful formation was not always readily achieved. A homogeneous gray liquid shows successful supraparticle formation (Supporting Information Figure 1B). Occasionally, the supraparticles precipitate after the formation process or during column purification, resulting in particle aggregates visible to the naked eye. We hypothesize that the lesser stability against aggregation is due to the type of amphiphiles present (saponin only vs a mixture of phospholipids and other bilayer-forming amphiphiles) and the higher ratio of hydrophobic particles to amphiphiles.

https://dx.doi.org/10.1021/acs.langmuir.9b03479
Langmuir 2020, 36, 3912−3923

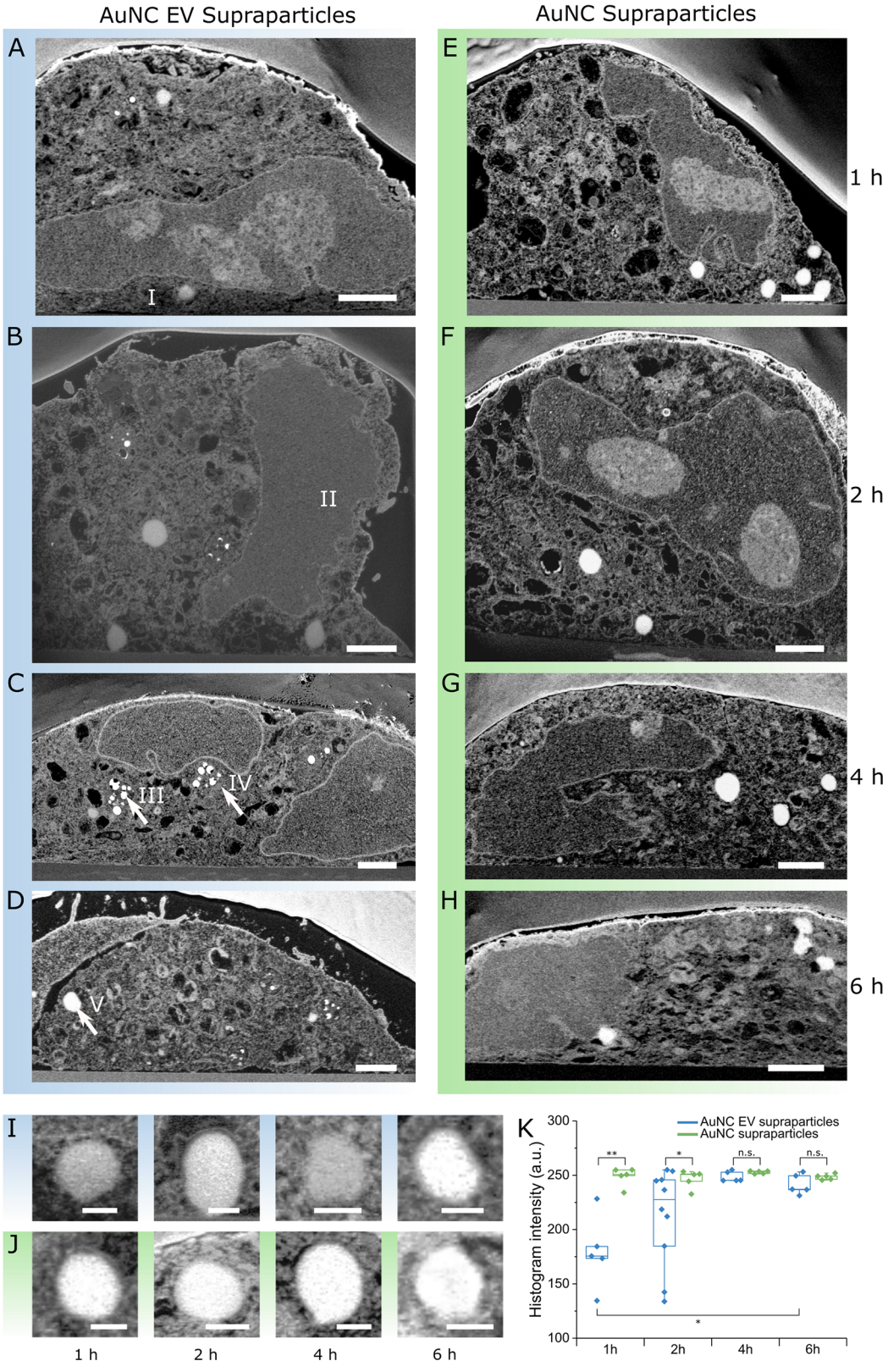

Figure 2. FIB-SEM imaging of the uptake comparison in MDA-MB-231 cells. (A−D) AuNC EV supraparticles. (E−H) AuNC supraparticles, with 1, 2, 4, and 6 h incubations respectively, scale bars = 2 μm. Roman numerals and arrows indicate exemplar structures of the cytoplasm (I), nucleus (II), AuNC EV supraparticles (III), endosome (IV), and lysosome (V). Lysosomal brightness analysis, with close-ups of lysosomes after 1, 2, 4, and 6 h for (I) AuNC EV supraparticles and (J) AuNC supraparticles, with scale bars = 500 nm. (K) Brightness analysis from center histograms' mean ± s.d. (n = 5, 2 h EVs, n = 10), *p < 0.05, ** p < 0.01, Welch's corrected t test between particle types, and Welch's Anova with the Games−Howell posthoc test for AuNC EVs over time. Histograms of all cell images are equalized to the 1 h AuNC EV supraparticles' image prior to close-up cropping.

https://dx.doi.org/10.1021/acs.langmuir.9b03479
Langmuir 2020, 36, 3912−3923

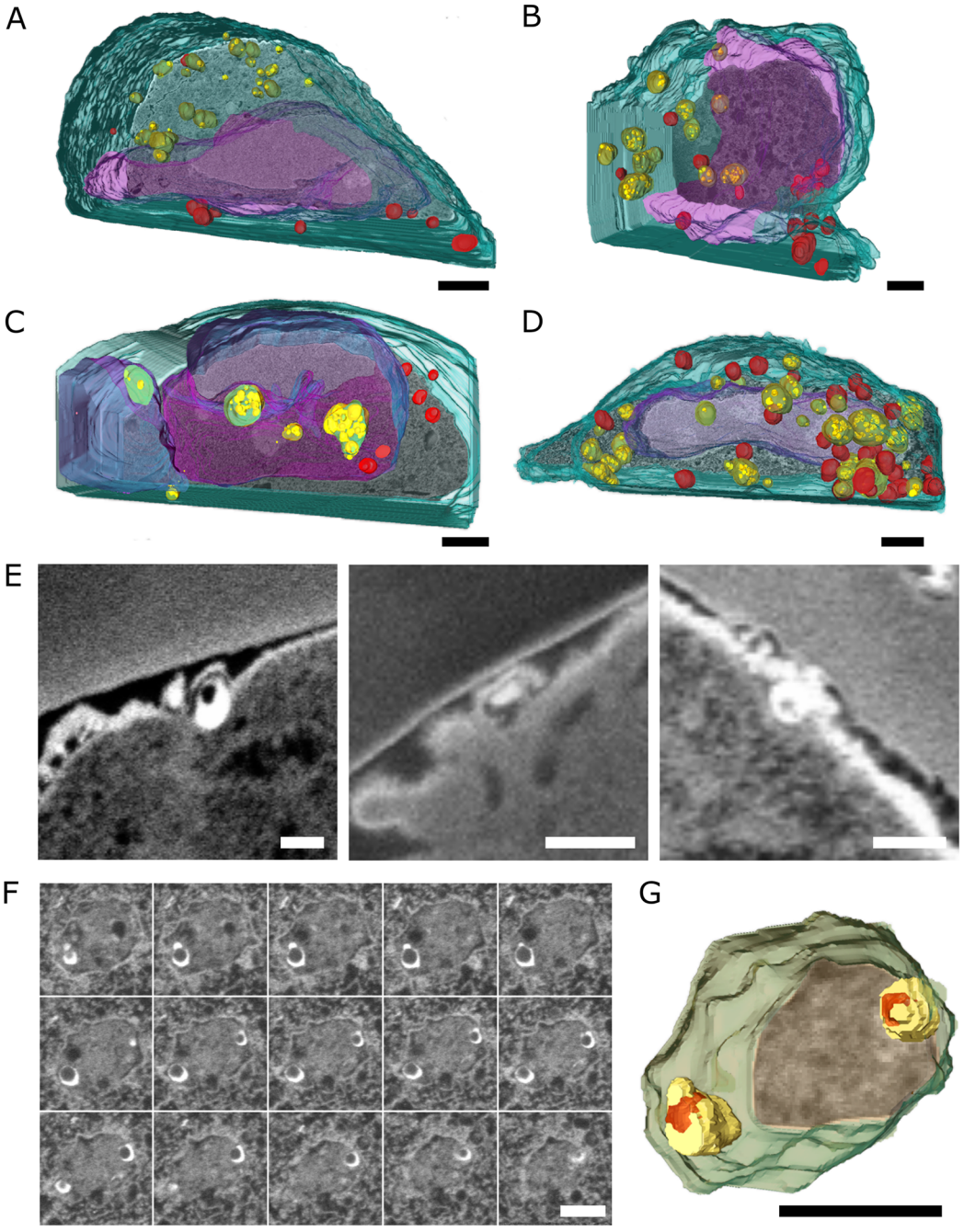

Figure 3. Three-dimensional reconstructions and close-up FIB-SEM imaging of AuNC EV supraparticle uptake. (A) 1, (B) 2, (C) 4, and (D) 6 h, with segmentation in the 3D reconstructions showing the cytoplasm (green), nucleus (purple), lysosomes (red), endosomes (orange), and AuNC EV supraparticles (yellow). Endosomal uptake of the particles can be seen over time with an increase in the lysosome presence, scale bars = 2 μm. (E) 1 h incubation, uptake events visible in three different cells of AuNC EV supraparticles with the cell membrane. (F) 2 h incubation with the AuNC EV supraparticles visible within an endosomal membrane, image stack left-to-right, top-to-bottom with a 20 nm slice thickness. (G) Three-dimensional reconstruction of the endosome stack in F showing the endosomal compartment in orange, the AuNC shell in yellow, and the supraparticle centers in red. Scale bars = 500 nm.

The self-assembled supraparticles were analyzed via dot blot, cryo-TEM, and FIB-SEM after cell uptake. Dot blots were performed to confirm that the EV AuNC particles still contained EV proteins after AuNC labeling and purification. The expression of CD63, CD81, and CD9, well-established EV markers,[40,41] was assessed and found to be abundant in native EVs, with the preservation of some of the signal for AuNC EV supraparticles, while no signal was seen for the EV-free supraparticle control (Supporting Information Figure 2).

The self-assembled structures were visualized by cryo-TEM, a technique that allows EM imaging in vitrified ice. This is beneficial compared to conventional TEM as the samples are not dried and self-assembled structures can therefore be visualized in their native hydration state. The images revealed the presence of spherical structures that visibly consist of small 1−3 nm AuNCs for both types of self-assembled supraparticles, with and without EVs (Figure 1H−I, additional images are shown in Supporting Information Figure 3A,B). Intriguingly, both supraparticle

https://dx.doi.org/10.1021/acs.langmuir.9b03479
Langmuir 2020, 36, 3912−3923

assemblies showed a smaller spherical area within them that was free of AuNCs. To make sure that this area was not just remaining THF solvent from the stock solution of AuNCs, we incubated the formed supraparticle solutions in a drying oven over a period of 1 h to evaporate remaining solvent. However, the inner empty sphere remained and was not different from that of the supraparticles formed without this drying process (Supporting Information Figure 4A). An alternative drying process was also tested by adding the supraparticle solutions to a rotation evaporator at a pressure of 20 mbar for 30 min, but the cryo-TEM images again showed this characteristic spherical area (Supporting Information Figure 4B).

Cell Uptake and Analysis. AuNC-based supraparticles are a powerful tool for in vitro detection as they are easily visualized with electron microscopy. We incubated purified and via filtration sterilized AuNC EV supraparticles and AuNC supraparticles with MDA-MB-231 cells and analyzed their uptake. Using an assay based on cell counting kit (CCK) 8, we detected no significant negative impact on cell viability for up to 6 h after incubation with supraparticles, either with or without EVs, against the native EV or PBS controls (Supporting Information Figure 5).

The two particle types were incubated with cells for different periods of time (1, 2, 4, and 6 h) to investigate and compare their uptake behavior over time, after which the cells were washed and fixed. Following heavy metal staining, dehydration, and resin embedding, the samples were imaged using FIB-SEM. We were able to visualize and segment the inner structure of the cells in high detail to track the uptake behavior of the supraparticles. We detected a strikingly different uptake behavior when AuNC EV supraparticles and AuNC supraparticles were compared, showing that the EVs strongly influenced how these complex structures were recognized and taken up by cells. An overview of the uptake between 1 and 6 h of the AuNC EV supraparticles in MDA-MB-231 cells is shown in Figure 2A−D, and that for the AuNC supraparticles is shown in Figure 2 E−H. Cells were milled perpendicular to the cell surface to expose and image the inner structure of the cells using a backscattered electron detector in SEM mode. The cell cytoplasm, nucleus, AuNC EV supraparticles, endosomes, and lysosomes can be seen as indicated by the arrows and Roman numerals I−V, respectively. Within the cells, the clear uptake of AuNC EV supraparticles is confirmed, as the gold labeling provides a very bright elemental contrast in the backscattered electron images. An example is indicated with a yellow arrow in Figure 2C. In contrast, no intact uptake was observed at any of the time points when the cells were incubated with AuNC supraparticles (Figure 2E−H).

This indicates that the AuNC supraparticles are not taken up by the cells while remaining intact or degrade very rapidly upon uptake.

Another clear difference for the comparison of EV-free and EV-containing supraparticle uptake studies was observed regarding the appearance of the lysosomes. After 1 h of incubation with AuNC supraparticles without EVs, already numerous very bright lysosomes (identified by their size and dense staining) can be seen inside the cell (Figure 2E). This implies the presence of AuNCs (or their aggregates) inside the lysosomes due to their high brightness in the backscattered electron images. This difference in lysosomal brightness is observed between the AuNC EV supraparticles' and AuNC supraparticles' uptake across the different time points (Figure 2I,J, respectively) during FIB-SEM imaging. To be able to compare the lysosomal brightness of these two experimental sets quantitatively, the histograms of the cell images were equalized using MATLAB to correct for differences in brightness and contrast imaging settings during acquisitions. After equalization, the images were cropped to the lysosomes and a local histogram was calculated from the central area of each lysosome for comparison. In addition, the cells and time points that were compared were all from the same experimental preparation batch to avoid differences in staining (and thus resulting brightness and contrast) influencing the analysis.

The resulting brightness of the lysosomes after incubation with AuNC supraparticles is high from the 1 h incubation time point onward, remaining more or less constant up to the final 6 h time point. A quantitative assessment of this can be seen in Figure 2K. However, for the AuNC EV supraparticles the brightness of the lysosomes is significantly lower after 1 h of incubation, with an increase in variability at the 2 h time point and finally similar accumulation into the lysosomes at 4 and 6 h. In summary, this indicates that a large number of AuNCs of the AuNC supraparticles without EVs can be found inside the lysosome from the earliest time point of 1 h onward, while for the AuNC EV supraparticles there is a more gradual trafficking to the lysosomes. This is indicated by the lower brightness at 1 h, increasing over 2−4 h to a similar end point as compared to the AuNC supraparticles.

To visualize the structure and uptake of the supraparticles in greater detail, image stacks were taken with a 90 nm spacing between slices. These were carefully aligned, and the cell structures were manually segmented into cytoplasm (green), nucleus (purple), lysosomes (red), endosomes (orange), and AuNC EV supraparticles (yellow), the result of which can be seen in Figure 3A−D for 1, 2, 4, and 6 h, respectively and Supporting Information movies 1−4. Significant endosomal uptake was already observed for the 1 h incubation time point with the AuNC EV supraparticles. Moreover, a few AuNC EV supraparticles can be seen in the cytoplasm and near the cell membrane. At 2 and 4 h time points, a clear localization of AuNC EV supraparticles in the endosomes is observed, and several lysosomes are visible within the cells, while at the 6 h time point both endosomes and lysosomes can be seen in high numbers as seen in Figure 3D.

Looking further into the early uptake of AuNC EV supraparticles, at the 1 h time point we imaged multiple cells, paying close attention to the presence of AuNC EV supraparticles close to the cell membrane. Due to the large number of washes involved in the preparation before FIB-SEM imaging, only AuNC EV supraparticles actually in the process of uptake would have been retained, while those that may be adsorbed or otherwise associated with the membrane would most likely have been removed during processing. Some of these uptake events are visualized in Figure 3E. These images all show AuNC EV supraparticles in very close proximity to the cell membrane with membrane wrapping around the particles, which indicates macropinocytosis as one of the uptake mechanisms.[42]

We set out to visualize the endosomal uptake in greater detail, as shown in Figure 3F,G. As seen in the image stack montage in Figure 3F, serial sectioning was performed on an endosome with AuNC EV supraparticles inside using a fine sectioning of 20 nm between slices. Here, it was observed that the AuNCs form a shell surrounding an inner lumen, similar to the EV membrane around its inner compartment. A 3D reconstruction of this endosome can be seen in Figure 3G with the endosomal compartment in orange, the AuNC shell in yellow, and the particle interior in red.

https://dx.doi.org/10.1021/acs.langmuir.9b03479
Langmuir 2020, 36, 3912−3923

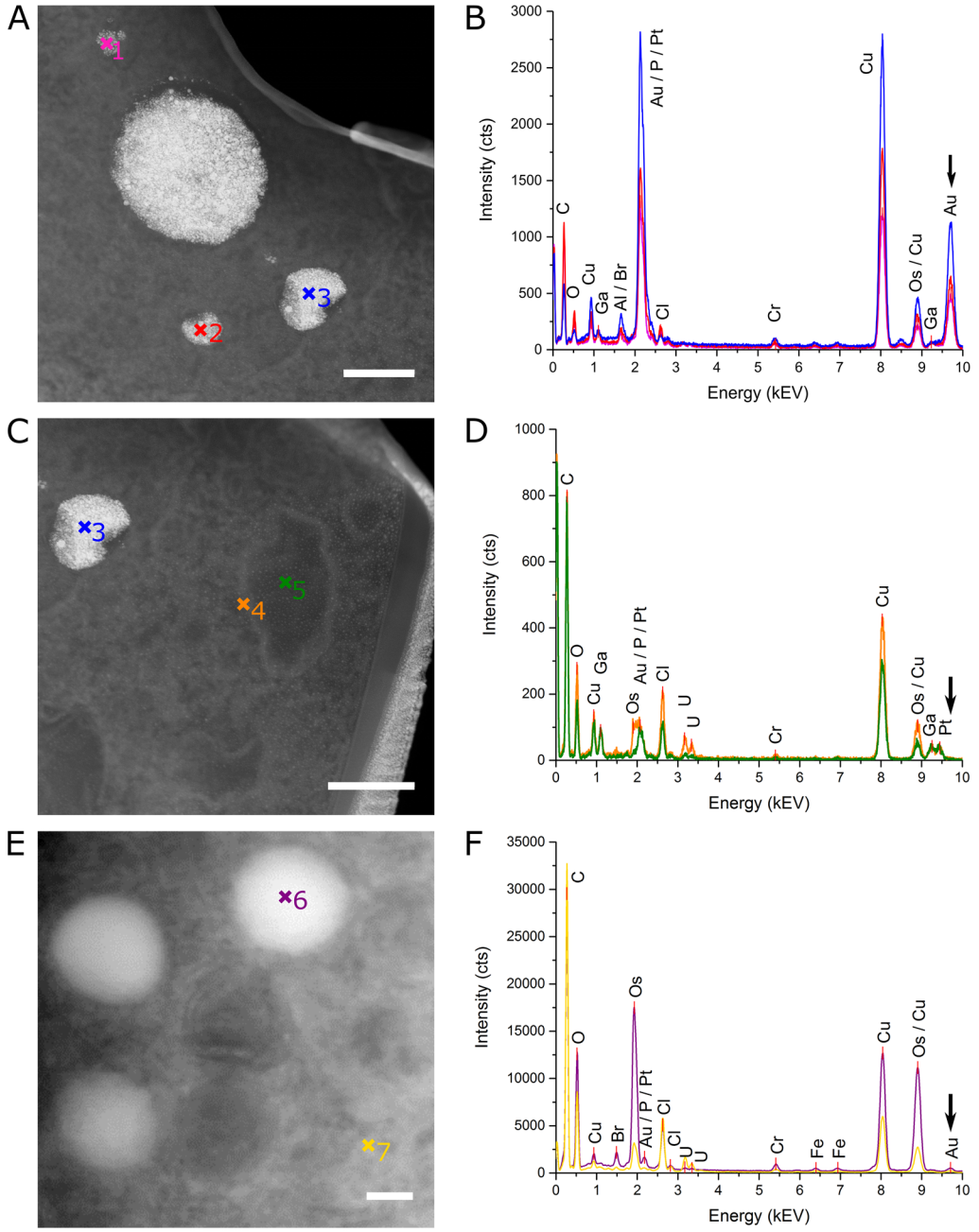

Figure 4. DF-STEM imaging and EDX analysis of FIB lift-out lamellae. (A, C) DF-STEM imaging after 4 h of incubation with AuNC EV supraparticles. A and C show close-ups of AuNC EV supraparticles within the cell with increasing detection of gold in the EDX spectra (B, 1−3) and no detectable gold away from the particles (D, 4−5). (E) DF-STEM imaging after 1 h of incubation with AuNC supraparticles showing bright lysosomes with a small amount of gold detectable within the lysosome by EDX (F, 6−7), where arrows indicate the position of the $L_{\alpha 1}$ shell excitation of gold at 9.7 keV. Scale bars = 250 nm.

Finally, to confirm the presence of gold within the AuNC EV supraparticles in situ and the presence of AuNC at the 1 h incubation time point in lysosomes for AuNC supraparticles, FIB lift-out sections of MDA-MB-231 cells incubated with the particles were prepared for dark-field scanning transmission electron microscopy (DF-STEM) imaging and high-resolution energy dispersive X-ray (EDX) analysis, as shown in Figure 4.

Due to the small amount of gold present, EDX analysis in the bulk cell sample during FIB-SEM would not have been accurate due to the high accelerating voltage needed, and thus large resulting X-ray generation volume, to excite the $L\alpha_1$ shell of gold. Therefore, lamellae were prepared by FIB lift-out to allow TEM and DF-STEM imaging and high-resolution EDX analysis as shown in Figure 4. During FIB lift-out, in a procedure similar to one we recently described,[43] a region of interest is approached using FIB serial sectioning, and a lamella is cut from the cell, lifted out using an Omniprobe needle (Oxford Instruments), and attached using platinum deposition to a lift-out TEM grid. The lamella is then thinned using the FIB to TEM electron transparency (approximately 100−120 nm), ensuring that the object of interest is contained within this section. We imaged these lamellae using DF-STEM (Figure 4A,C) and were able to confirm the presence of gold within the AuNC EV supraparticles with EDX analysis as well as detect small amounts within the

https://dx.doi.org/10.1021/acs.langmuir.9b03479
Langmuir 2020, 36, 3912−3923

lysosomes after 1 h of incubation with AuNC supraparticles. Spectra 1−3 in Figure 4B show that the gold signal increases with particle size, while no gold is detected away from the particles (shown in spectra 4 and 5 in Figure 4C).

A notable increase in the uranium elemental signal is observed when collecting a spectrum on a membranous structure in the cytoplasm (spectrum 4) due to the heavy metal staining protocol, which illustrates the high resolution of the EDX acquisition. As shown in Figure 4E, a lamella was prepared after a 1 h incubation with AuNC supraparticles, isolating a region of interest containing numerous bright lysosomes. EDX analysis confirmed the presence of a small amount of gold within these lysosomes, confirming the early uptake as shown in Figure 2K.

CONCLUSIONS

We have demonstrated the first method for the self-assembly of supraparticles with breast cancer cell-derived EVs and hydrophobic AuNCs, characterized them with cryo-TEM, and analyzed their cellular uptake via FIB-SEM and 3D reconstructions. We showed clustering of the AuNC EV supraparticles in endosomes and later degradation in lysosomes. The isolation of cell lamellas via FIB lift-out and subsequent DF-STEM imaging and EDX analysis showed the presence of gold in the AuNC EV supraparticles inside the cell. In comparison, AuNC supraparticles (formed without the natural EV component) were not sufficiently stable for cellular uptake tracking. No intact AuNC supraparticles were observed within the cells, but the presence of gold was detectable in the lysosomes within 1 h.

In summary, we have demonstrated the role that EVs can play in making a difference in the cellular uptake of nanoparticles. We have also shown that the assembly of AuNCs with EVs allows detailed tracking and visualization within cells via FIB-SEM imaging, and this method may be instrumental in a variety of future applications, such as mechanistic uptake studies of EV-based diagnostic and therapeutic technologies. This is the first proof of concept of EV-based AuNC supraparticles and exemplifies the powerful combination of complex biological entities with the versatility of nanoparticles. Moreover, we have demonstrated an easily accessible route to combining hydrophobic nanoparticles with EVs. While exceeding the scope of this study, this method has a high potential for combining the manifold theranostic functionalities of different nanoparticles reported in the literature with the biocompatibility and targeting properties of EVs.

METHODS

Cell Culture and EV Extraction. MDA-MB-231 breast cancer cells were obtained from the ATCC (Manassas, VA, USA) and maintained in DMEM supplemented with 10% (v/v) FBS, 20 mM HEPES, and penicillin/streptomycin (all from Gibco). To maximize the production of EVs, they were adapted to nonadherent culture to allow high-density growth. The cells were cultured at 37 °C and 5% CO_2, and their medium was changed every 2 days. To obtain EVs, cells were cultured to a concentration of approximately 1×10^6 cells/mL. Cells were pelleted via centrifugation at 300*g*. The cells were resuspended in DMEM supplemented with only 20 mM HEPES and penicillin/streptomycin and incubated for 2 days. Afterward, the conditioned medium was collected by the centrifugation of cell suspensions at 1500*g* for 5 min.

The medium was then filtered over a bottle top filter with a 0.45 μm pore size (VWR, U.K.) and concentrated using ultrafiltration (Amicon Ultra-15, 100 kDa).

The concentrated medium was purified by size exclusion chromatography. The concentrated medium (500 μL) was loaded onto a 30-cm-long, 1-cm-diameter column containing Sepharose CL-2B (Sigma-Aldrich, U.K.). One milliliter fractions were collected, and the EV-containing fractions were determined via data correlation of a BCA assay (Thermo Fisher) and NTA (Malvern). EVs were snap frozen and stored at −80 °C until further use.

AuNC Synthesis. All chemicals were obtained from Sigma-Aldrich U.K. and were of the highest purity unless otherwise stated. $HAuCl_4 \cdot 2H_2O$ (0.1576 g, 0.4 mmol) was dissolved in 5 mL of Milli Q water. TOAB (0.2558 g, 0.47 mmol) was dissolved in 10 mL of toluene. Both solutions were combined in a 25 mL round-bottomed flask and stirred at 1100 rpm for 15 min. By this time, the bottom phase became clear and colorless due to the gold salt transferring into the toluene phase. The bottom phase was removed with a syringe. The toluene phase was cooled to 0 °C and purged with nitrogen for 30 min. Octanethiol (0.2 mL, 1.2 mmol) was added, and stirring was reduced to 30 rpm. A reduction in stirring speed results in a higher yield of smaller clusters.[38] The solutions turned yellow over a period of 5 min and became clear after 1 h. The stirring speed was increased to 1100 rpm, and freshly prepared $NaBH_4$ solution was added immediately at once. To prepare the $NaBH_4$ solution, $NaBH_4$ (0.1550 g, 4 mmol) was added to 7 mL of ice-cold Milli-Q water. The reaction was stirred overnight under a N_2 atmosphere at 0 °C. Afterward, the water phase was removed with a syringe and the reaction vessel was flushed with 5 mL of toluene to bring all AuNCs to the bottom of the vessel.

The toluene phase was removed by vacuum distillation using a dry ice cooler under gentle stirring and using a heat gun to gently heat the mixture to aid distillation. After removal of the toluene, the vessel was kept under vacuum for another 10 min to dry.

The AuNCs were resuspended in 20 mL of ethanol, filtered over cotton, and washed another three times on cotton with ethanol. The clusters were removed from the cotton by flushing with toluene and were further dried by vacuum distillation as above. The clusters were further dried overnight under vacuum, and the clusters were analyzed by TEM (JEM JEOL 2100F, FEI TITAN) to determine their size distribution.

Supraparticle Formation. Supraparticles containing EVs were synthesized using 500 μL of purified EVs in PBS in a glass vial. The concentration of EVs ranged from 7×10^{11} to 2×10^{12} particles/mL. A saponin stock solution (40 μL, 3.5 mg/mL) in Milli-Q water was added to the EV suspension. Afterward, 40 μL of an AuNC solution (10 mg/mL) in THF was added. This mixture was then added to a commercially available size exclusion chromatography column (qEV, Izon Sciences Ltd.). The suspension (500 μL) was added to a qEV column, and the entire gray band was collected from the column. Typically, the supraparticles would elute in fractions 7 and 8 when collecting 500 μL fractions. Supraparticles without EVs were synthesized using the same protocol, but instead using 500 μL of PBS rather than 500 μL of EVs in PBS.

Cell Incubation with Supraparticles and Preparation for FIB-SEM. Glass coverslips (10 mm; VWR, U.K.) were sterilized by washing in 70% ethanol, washed twice in PBS, and placed in a 24-well plate. Coverslips were precoated in full cell culture medium for 1 h at 37 °C, 5% CO_2. MDA-MB-231 cells grown to 80% confluency in a T75 culture flask were harvested.

Cells were seeded at 15 000 cells/cm^2 and allowed to adhere overnight. AuNC EV and EV-free supraparticles at 0.4×10^{11}−1×10^{11} p/mL were sterile filtered using a 0.45 μm syringe filter. A volume of 120 μL was added to each well (PBS only for controls) containing 1 mL of complete medium.

The cells and particles were incubated for 1, 2, 4, or 6 h, respectively. The experiment was performed in duplicate, and only a 6 h time point was used for the controls without particles. At each time point, cultures were washed with PBS and fixed in 4% EM-grade PFA (Electron Microscopy Sciences) for 15 min at 37 °C, 5% CO_2. After fixing, the slides were washed another three times in PBS and kept covered overnight in PBS in the refrigerator.

For FIB-SEM preparation, the samples were washed for 2 × 5 min in 0.1 M cacodylate buffer (Electron Microscopy Sciences, 0.2 M stock) in dH_2O. The samples were postfixed for 1 h in 2.5% EM-grade glutaraldehyde (Electron Microscopy Sciences, 16% stock) in 0.1 M

https://dx.doi.org/10.1021/acs.langmuir.9b03479
Langmuir 2020, 36, 3912−3923

cacodylate buffer. After further washing for 2 × 5 min in 0.1 M cacodylate, the samples were stained for 1 h in 1% OsO_4 (Electron Microscopy Sciences, 4% stock) in 0.1 M cacodylate and washed 2 × 5 min in dH_2O. Further staining was performed for 1 h in 1% tannic acid (0.2 μm syringe filtered) and 2.5 h in uranyl acetate (0.2 μm syringe filtered) in dH_2O with 2 × 5 min washes in dH_2O in between. The samples were serially dehydrated using an ethanol/water gradient of 20, 30, 50 and 70% ethanol for 2 × 5 min each and kept on 70% ethanol overnight at room temperature.

The samples were further dehydrated by 2 × 5 min washes in 80 and 90% ethanol and 4 × 5 min washes in 100% ethanol. Next, the samples were resin embedded by gradient infiltration of 2.5 h each with 3:1, 2:1, and 1:1 (v/v) ethanol and epoxy resin (epoxy embedding medium kit, Sigma-Aldrich U.K.) and 1:2 overnight and were covered at room temperature.

The next day, the resin infiltration was finalized by 2 × 2.5 h incubation in full resin and the removal of excess resin by rapid ethanol spraying and blotting on paper for minimal resin embedding. The coverslips were transferred to PDMS mats and cured for 72 h in an oven at 60 °C. Prior to imaging, the coverslips were mounted on standard SEM stubs using double-sided carbon tape and sputter coated with 20 nm of chromium (Quorum Q150T S).

FIB-SEM Imaging and Three-Dimensional Reconstruction. Cells were imaged using an Auriga Zeiss Crossbeam and a sample tilt of 54° with 36° image tilt correction and a 5 mm working distance. Coarse FIB milling was performed at 2 nA:30 kV and fine milling for serial sectioning at 1 nA:30 kV. SEM images were taken at a 1.6 kV accelerating voltage using a back-scattered electron detector. For 3D reconstruction, serial images stacks were taken with a 90 nm interval and automatically aligned using Fiji (ImageJ, StackReg plugin) and further manually aligned and segmented using Amira 5.3.2 (FEI).

TEM and Cryo-TEM. Copper grids (CF200-Cu, Electron Microscopy Sciences) and holey carbon grids (HC200-Cu, Electron Microscopy Sciences) were plasma treated (15 s, O_2/H_2) on a Gatan Solaris plasma cleaner. Samples for TEM were prepared by adding a 4 μL sample to the grid and incubating for 30 s, after which excess solution was blotted off with filter paper, and the sample was dried overnight. Samples for cryo-TEM were prepared with a Leica EM GP automatic plunge freezer. Samples (4 μL) were added to a grid in an environmental chamber (relative humidity 90%, temperature 20 °C). Excess suspension was blotted on filter paper, and the obtained film was vitrified in liquid ethane. Samples were stored in liquid nitrogen until the day of use.

TEM samples were imaged on a JEOL 2100F or JEOL 2100Plus using 200 kV, while cryo-TEM samples were imaged only on the JEOL 2100Plus using 200 kV with the minimum dose system. Cryo-TEM samples were imaged at −170 °C on a Gatan914 cryo-holder for cryo-TEM imaging. Micrographs were taken using the Gatan Orius SC1000 camera at a magnification of either 30 000× or 15 000×.

Lift-Out Preparation and STEM/EDX. Lamellae of MDA-MB-231 cells incubated with supraparticles prepared with or without EVs were prepared using FIB-SEM lift-out for further analysis by TEM/STEM and EDX using a Helios Nanolab 600 (FEI) system equipped with a micromanipulator (Omniprobe, Oxford Instruments plc, U.K.). The samples were imaged with SEM at 0.17 nA:2 kV, and lamellae were prepared using 30 kV FIB milling at various currents from 28 pA to 2.8 nA. A trench was milled in the cell until a region of interest was observed in SEM imaging. A second trench was milled behind the region of interest until a lamella of 1−1.5 μm thickness remained. Platinum was deposited using a gallium ion-assisted gas injection system (GIS, 93−0.28 nA) on top of the lamella to a thickness of 1 to 2 μm. The lamella was freed by further milling on either side, except the base, and a micromanipulator needle was attached to a corner by further platinum deposition. The base of the lamella was cut, and the lamella was gently lifted out using the micromanipulator and guided to a three-pronged lift-out grid (Omniprobe, EM Sciences). The lamella was attached to one of the posts by platinum deposition, and the needle was cut loose. By FIB polishing down to 5 kV and 8 pA, the lamella was thinned to electron transparency, 100−120 nm, using SEM imaging to ensure that the region of interest was conserved within the lamella.

The lift-out grid was transferred to a JEOL 2100F 200 kV TEM where the lamella was observed and further imaged using STEM mode and a dark-field detector at a 15° sample tilt. EDX was performed in STEM mode using INCA software (Oxford Instruments). Peaks were assigned using the Bruker X-ray energies table (Bruker, Berlin, Germany).

For the verification of the presence of gold in the AuNC EV supraparticles, the acquisition time was 30 s. To assess the presence of gold in lysosomes for the EV-free AuNC supraparticle sample, an acquisition time of 60 s was used.

Histogram Analysis. For equalization and comparison of the lysosomal brightness in the backscattered electron SEM images, the images were cropped to the cell boundaries and imported into MATLAB (R2016B). A 1 h AuNC EV supraparticle image was taken as reference, and the histograms of the other images were matched using the built-in "imhistmatch" function. The equalized images were imported back into Fiji (ImageJ) and cropped to the lysosomes, for 5 lysosomes per condition except for the 2 h AuNC EV sample, in which 10 lysosomes were analyzed due to the large observed variance. A histogram was calculated for the central area of a lysosome at each time point, and the particle type, means, and standard deviations of the histograms were plotted in Origin (Origin Pro 2017). Welch's corrected t tests were performed in Origin between particle types for means comparison and a Welch's Anova with Games−Howell post hoc test in SPSS (SPSS 25, IBM) to compare means over time for the AuNC EVs, both taking into account unequal variance and unequal sample size.

NTA Measurements. EV particle concentrations and size distribution were measured on a Nanosight NS300 (Malvern) equipped with a 532 nm laser and a sCMOS camera. Samples were diluted 1000-fold in PBS to yield a concentration of 10^8−10^9 particles/mL. Three 30 s videos were recorded per sample, using NTA software V3.0 with a camera level set to 15 and a detection threshold set to 5.

BCA Assay. A BCA protein quantification assay kit (Thermo Fisher U.K.) was used according to the manufacturer's instructions to quantify the amount of protein in each of the 26 sequential 1 mL elution fractions of the size exclusion chromatographic purification of MDA-MB-231 EVs. An eight-point BSA calibration curve was made between 0 and 2 mg/mL, measured in duplicate, and used to quantify the amount of protein in the sample fractions (mean of $n = 2$) upon read out of the assay absorbance at 562 nm using a UV−vis plate reader (SpectraMax M5, Molecular Devices).

CCK-8 Assay. To test the potential cytotoxicity of the EVs or supraparticles, a CCK-8 (Sigma-Aldrich, U.K.) cell viability assay was performed. MDA-MB-231 cells were cultured to 80% confluency in a T75 culture flask, trypsinized and seeded at 10 000 cells/well in a 96-well tissue culture plate, and incubated overnight. A stock of MDA-MB-231 EVs at 7 × 10^{11} particles/mL was used to prepare AuNC EV supraparticles and AuNC supraparticles. The particles were sterile-filtered using a 0.45 μm Millex PVDF mini syringe filter and premixed with complete media (around 3.5 × 10^{11} particles/mL due to qEV column dilution, corrected for native EVs), equivalent to the FIB-SEM assays. The particles were further diluted 2- and 10-fold to assess potential differences in cytotoxicity.

Cells with complete media and cells in complete media with an equivalent of PBS were used as controls. The cells were incubated for 6 h, washed once in PBS, and incubated for another 3 days before assessing viability using the CCK-8 assay. Substrate (10 μL) in 190 μL of complete media was added to each well (premixed for all wells), including wells with a CCK-8 background control (no cells). The end-point absorbance was read using a UV−vis plate reader (SpectraMax M5, Molecular Devices) at 450 nm after 3 h of incubation. The assay was performed with three technical and biological replicates.

Dot Blots. A stock of MDA-MB-231 EVs of 7 × 10^{11} particles/mL was used to prepare AuNC EV supraparticles as described above, and EV samples from the same batch were used as a control, diluted 2-fold in PBS to match the dilution from the qEV column used to purify the AuNC EV supraparticles. AuNC supraparticles were prepared in a similar way using PBS instead of the EV stock. A nitrocellulose membrane (0.45 μm, Bio-Rad) was soaked in 1× TBS (tris-buffered

https://dx.doi.org/10.1021/acs.langmuir.9b03479
Langmuir 2020, 36, 3912−3923

saline, 20× stock diluted in Milli-Q water, Bio-Rad) for 10 min. The BioDot apparatus (Bio-Rad) was assembled according to the manufacturer's instructions, and 200 μL was loaded per sample and per antibody target in triplicate, adding TBS to the remaining empty wells. The wells were allowed to drain for 1 to 2 h, after which the wells were washed three times with TBS and drained by vacuum. The membrane was retrieved from the apparatus, marked with a pencil, and cut into strips pertaining to each antibody target. The membranes were blocked in 5% skimmed milk in TBS-T (1× TBS with 0.1% Tween 20) solution for 1 h at RT. After blocking, the membranes were washed three times in TBS-T for 10 min at RT and incubated overnight at 4 °C while being shaken with the respective primary antibody.

The primary antibodies used were anti-CD63 (Invitrogen, 10628D), anti-CD81 (Invitrogen, 10630D), and anti-CD9 (Invitrogen, 10626D), diluted 1:1000 in 5% (w/v) BSA in TBS-T. The next day, the membranes were washed three times in TBS-T for 10 min at RT and incubated for 1 h at RT with the secondary antibody (IRDye 800CW Donkey anti-Mouse IgG, Li-Cor) 1:10 000 in 5% (w/v) BSA in TBS-T. The membranes were finally washed three times in TBS-T for 10 min at RT before imaging using the Li-Cor imaging system.

■ ASSOCIATED CONTENT

Supporting Information

The Supporting Information is available free of charge at https://pubs.acs.org/doi/10.1021/acs.langmuir.9b03479.

AuNC supraparticle and AuNC EV supraparticle formation photographs, dot blot EV marker screening, additional cryo-TEM images of AuNC EV supraparticles and AuNC supraparticles, postoven and rotary evaporation drying images of AuNC EV supraparticles, CCK-8 viability assay results, and descriptions of movies showing the full SEM image stack obtained during FIB-SEM serial acquisition and the resulting three-dimensional reconstructions (PDF)

One hour uptake of AuNC EV supraparticles (MP4)

Two hour uptake of AuNC EV supraparticles (MP4)

Three hour uptake of AuNC EV supraparticles (MP4)

Four hour uptake of AuNC EV supraparticles (MP4)

■ AUTHOR INFORMATION

Corresponding Author

Molly M. Stevens − *Department of Materials, Department of Bioengineering, and Institute of Biomedical Engineering, Imperial College London, London SW7 2AZ, United Kingdom; Department of Medical Biochemistry and Biophysics, Karolinska Institutet, Stockholm SE-171 77, Sweden;* orcid.org/0000-0002-7335-266X; Email: m.stevens@imperial.ac.uk

Authors

Ulrike Kauscher − *Department of Materials, Department of Bioengineering, and Institute of Biomedical Engineering, Imperial College London, London SW7 2AZ, United Kingdom;* orcid.org/0000-0002-2681-5692

Jelle Penders − *Department of Materials, Department of Bioengineering, and Institute of Biomedical Engineering, Imperial College London, London SW7 2AZ, United Kingdom;* orcid.org/0000-0002-5232-917X

Anika Nagelkerke − *Department of Materials, Department of Bioengineering, and Institute of Biomedical Engineering, Imperial College London, London SW7 2AZ, United Kingdom; University of Groningen, Groningen Research Institute of Pharmacy, Pharmaceutical Analysis, NL-9700 AD Groningen, The Netherlands*

Margaret N. Holme − *Department of Materials, Department of Bioengineering, and Institute of Biomedical Engineering, Imperial College London, London SW7 2AZ, United Kingdom; Department of Medical Biochemistry and Biophysics, Karolinska Institutet, Stockholm SE-171 77, Sweden;* orcid.org/0000-0002-7314-9493

Valeria Nele − *Department of Materials, Department of Bioengineering, and Institute of Biomedical Engineering, Imperial College London, London SW7 2AZ, United Kingdom*

Lucia Massi − *Department of Materials, Department of Bioengineering, and Institute of Biomedical Engineering, Imperial College London, London SW7 2AZ, United Kingdom*

Sahana Gopal − *Department of Materials, Department of Bioengineering, and Institute of Biomedical Engineering, Imperial College London, London SW7 2AZ, United Kingdom*

Thomas E. Whittaker − *Department of Materials, Department of Bioengineering, and Institute of Biomedical Engineering, Imperial College London, London SW7 2AZ, United Kingdom*

Complete contact information is available at: https://pubs.acs.org/10.1021/acs.langmuir.9b03479

Author Contributions

#These authors contributed equally.

Notes

The authors declare no competing financial interest.

Raw data are available on request from rdm-enquiries@imperial.ac.uk

■ ACKNOWLEDGMENTS

U.K. acknowledges support from the Deutsche Forschungsgemeinschaft (KA 4370/1-1). J.P. acknowledges funding from the NanoMed Marie Skłodowska-Curie ITN from the H2020 program under grant number 676137. A.N. and M.M.S. acknowledge support from the GlaxoSmithKline Engineered Medicines Laboratory. M.N.H. also acknowledges support from the Swiss National Science Foundation (P300PA_171540) and support from the FP7Marie Curie Intra-European Fellowship "SMase LIPOSOME" (626766). M.N.H. and M.M.S. acknowledge financial support by the Swedish Foundation of Strategic Research in the Industrial Research Centre, FoRmulaEx − Nucleotide Functional Drug Delivery (IRC15-0065). V.N. acknowledges support from the Ermenegildo Zegna Founder's Scholarship Program and the Rosetrees Trust. L.M. acknowledges funding from the European Union's Horizon 2020 research and innovation programme under Marie Skłodowska-Curie grant agreement number 642414. S.G. acknowledges funding from the Department of Medicine and the Department of Bioengineering, Imperial College London. T.E.W acknowledges support from the Rosetrees Trust and the EPSRC. M.M.S. acknowledges a Wellcome Trust Senior Investigator Award (098411/Z/12/Z). The authors thank Dr. Colleen Loynachan and Mr. Charlie Winter for assistance with the Dot Blots, Dr. Qu Chen for assistance with TEM imaging, and the Harvey Flower Micro characterization Suite at the Department of Materials, Imperial College, for their support.

■ ABBREVIATIONS

AuNC, gold nanoclusters; EV, extracellular vesicle; FIB-SEM, focused ion beam-scanning electron microscopy; DF, dark field; (S)TEM, (scanning) transmission electron microscopy; EDX, energy-dispersive X-ray spectroscopy; NTA, nanoparticle tracking analysis; UV−vis, ultraviolet−visible; PBS, phosphate-

buffered saline; DMEM, Dulbecco's Modified Eagle's Medium; FBS, fetal bovine serum; CCK8, cell counting kit 8; TBS, (tris-buffered saline); TBS-T, (tris-buffered saline with 0.1% Tween 20)

REFERENCES

(1) Fuhrmann, G.; Herrmann, I. K.; Stevens, M. M. Cell-Derived Vesicles for Drug Therapy and Diagnostics: Opportunities and Challenges. *Nano Today* **2015**, *10* (3), 397−409.

(2) Armstrong, J. P. K.; Stevens, M. M. Strategic Design of Extracellular Vesicle Drug Delivery Systems. *Adv. Drug Delivery Rev.* **2018**, *130*, 12−16.

(3) Armstrong, J. P. K.; Holme, M. N.; Stevens, M. M. Re-Engineering Extracellular Vesicles as Smart Nanoscale Therapeutics. *ACS Nano* **2017**, *11* (1), 69−83.

(4) Février, B.; Raposo, G. Exosomes: Endosomal-Derived Vesicles Shipping Extracellular Messages. *Curr. Opin. Cell Biol.* **2004**, *16* (4), 415−421.

(5) Raposo, G.; Nijman, H. W.; Stoorvogel, W.; Liejendekker, R.; Harding, C. V.; Melief, C. J.; Geuze, H. J. B Lymphocytes Secrete Antigen-Presenting Vesicles. *J. Exp. Med.* **1996**, *183* (3), 1161.

(6) Chaput, N.; Théry, C. Exosomes: Immune Properties and Potential Clinical Implementations. *Semin. Immunopathol.* **2011**, *33* (5), 419−440.

(7) Wu, Y.; Deng, W.; Klinke II, D. J. Exosomes: Improved Methods to Characterize Their Morphology, RNA Content, and Surface Protein Biomarkers. *Analyst* **2015**, *140* (19), 6631−6642.

(8) van Niel, G.; D'Angelo, G.; Raposo, G. Shedding Light on the Cell Biology of Extracellular Vesicles. *Nat. Rev. Mol. Cell Biol.* **2018**, *19* (4), 213−228.

(9) Vader, P.; Breakefield, X. O.; Wood, M. J. A. Extracellular Vesicles: Emerging Targets for Cancer Therapy. *Trends Mol. Med.* **2014**, *20* (7), 385−393.

(10) Paolicelli, R. C.; Bergamini, G.; Rajendran, L. Cell-to-Cell Communication by Extracellular Vesicles: Focus on Microglia. *Neuroscience* **2019**, *405*, 148−157.

(11) Krämer-Albers, E.-M.; Hill, A. F. Extracellular Vesicles: Interneural Shuttles of Complex Messages. *Curr. Opin. Neurobiol.* **2016**, *39*, 101−107.

(12) Vader, P.; Mol, E. A.; Pasterkamp, G.; Schiffelers, R. M. Extracellular Vesicles for Drug Delivery. *Adv. Drug Delivery Rev.* **2016**, *106*, 148−156.

(13) Fuhrmann, G.; Serio, A.; Mazo, M.; Nair, R.; Stevens, M. M. Active Loading into Extracellular Vesicles Significantly Improves the Cellular Uptake and Photodynamic Effect of Porphyrins. *J. Controlled Release* **2015**, *205*, 35−44.

(14) Zhuang, X.; Xiang, X.; Grizzle, W.; Sun, D.; Zhang, S.; Axtell, R. C.; Ju, S.; Mu, J.; Zhang, L.; Steinman, L.; et al. Treatment of Brain Inflammatory Diseases by Delivering Exosome Encapsulated Anti-Inflammatory Drugs From the Nasal Region to the Brain. *Mol. Ther.* **2011**, *19* (10), 1769−1779.

(15) Sun, D.; Zhuang, X.; Xiang, X.; Liu, Y.; Zhang, S.; Liu, C.; Barnes, S.; Grizzle, W.; Miller, D.; Zhang, H.-G. A Novel Nanoparticle Drug Delivery System: The Anti-Inflammatory Activity of Curcumin Is Enhanced When Encapsulated in Exosomes. *Mol. Ther.* **2010**, *18* (9), 1606−1614.

(16) El-Andaloussi, S.; Lee, Y.; Lakhal-Littleton, S.; Li, J.; Seow, Y.; Gardiner, C.; Alvarez-Erviti, L.; Sargent, I. L.; Wood, M. J. A. Exosome-Mediated Delivery of SiRNA in Vitro and in Vivo. *Nat. Protoc.* **2012**, *7* (12), 2112−2126.

(17) Alvarez-Erviti, L.; Seow, Y.; Yin, H.; Betts, C.; Lakhal, S.; Wood, M. J. A. Delivery of SiRNA to the Mouse Brain by Systemic Injection of Targeted Exosomes. *Nat. Biotechnol.* **2011**, *29* (4), 341−345.

(18) Saari, H.; Lázaro-Ibáñez, E.; Viitala, T.; Vuorimaa-Laukkanen, E.; Siljander, P.; Yliperttula, M. Microvesicle- and Exosome-Mediated Drug Delivery Enhances the Cytotoxicity of Paclitaxel in Autologous Prostate Cancer Cells. *J. Controlled Release* **2015**, *220*, 727−737.

(19) Tang, K.; Zhang, Y.; Zhang, H.; Xu, P.; Liu, J.; Ma, J.; Lv, M.; Li, D.; Katirai, F.; Shen, G.-X.; et al. Delivery of Chemotherapeutic Drugs in Tumour Cell-Derived Microparticles. *Nat. Commun.* **2012**, *3* (1), 1282.

(20) Silva, A. K. A.; Kolosnjaj-Tabi, J.; Bonneau, S.; Marangon, I.; Boggetto, N.; Aubertin, K.; Clément, O.; Bureau, M. F.; Luciani, N.; Gazeau, F.; et al. Magnetic and Photoresponsive Theranosomes: Translating Cell-Released Vesicles into Smart Nanovectors for Cancer Therapy. *ACS Nano* **2013**, *7* (6), 4954−4966.

(21) King, H. W.; Michael, M. Z.; Gleadle, J. M. Hypoxic Enhancement of Exosome Release by Breast Cancer Cells. *BMC Cancer* **2012**, *12* (1), 421.

(22) Whiteside, T. L. Tumor-Derived Exosomes and Their Role in Cancer Progression. *Adv. Clin. Chem.* **2016**, *74*, 103−141.

(23) Costa-Silva, B.; Aiello, N. M.; Ocean, A. J.; Singh, S.; Zhang, H.; Thakur, B. K.; Becker, A.; Hoshino, A.; Mark, M. T.; Molina, H.; et al. Pancreatic Cancer Exosomes Initiate Pre-Metastatic Niche Formation in the Liver. *Nat. Cell Biol.* **2015**, *17* (6), 816−826.

(24) Hoshino, A.; Costa-Silva, B.; Shen, T.-L.; Rodrigues, G.; Hashimoto, A.; Tesic Mark, M.; Molina, H.; Kohsaka, S.; Di Giannatale, A.; Ceder, S.; et al. Tumour Exosome Integrins Determine Organotropic Metastasis. *Nature* **2015**, *527* (7578), 329−335.

(25) Howes, P. D.; Rana, S.; Stevens, M. M. Plasmonic Nanomaterials for Biodiagnostics. *Chem. Soc. Rev.* **2014**, *43* (11), 3835−3853.

(26) de la Rica, R.; Chow, L. W.; Horejs, C.-M.; Mazo, M.; Chiappini, C.; Pashuck, E. T.; Bitton, R.; Stevens, M. M. A Designer Peptide as a Template for Growing Au Nanoclusters. *Chem. Commun.* **2014**, *50* (73), 10648−10650.

(27) Hembury, M.; Chiappini, C.; Bertazzo, S.; Kalber, T. L.; Drisko, G. L.; Ogunlade, O.; Walker-Samuel, S.; Krishna, K. S.; Jumeaux, C.; Beard, P.; et al. Gold-Silica Quantum Rattles for Multimodal Imaging and Therapy. *Proc. Natl. Acad. Sci. U. S. A.* **2015**, *112* (7), 1959−1964.

(28) Klingberg, H. B.; Oddershede, L.; Loeschner, K.; Larsen, E. H.; Loft, S.; Møller, P. Uptake of Gold Nanoparticles in Primary Human Endothelial Cells. *Toxicol. Res. (Cambridge, U. K.)* **2015**, *4* (3), 655−666.

(29) Dykman, L. A.; Khlebtsov, N. G. Uptake of Engineered Gold Nanoparticles into Mammalian Cells. *Chem. Rev.* **2014**, *114* (2), 1258−1288.

(30) Wintzheimer, S.; Granath, T.; Oppmann, M.; Kister, T.; Thai, T.; Kraus, T.; Vogel, N.; Mandel, K. Supraparticles: Functionality from Uniform Structural Motifs. *ACS Nano* **2018**, *12* (6), 5093−5120.

(31) Yang, F.; Skripka, A.; Tabatabaei, M. S.; Hong, S. H.; Ren, F.; Benayas, A.; Oh, J. K.; Martel, S.; Liu, X.; Vetrone, F.; et al. Multifunctional Self-Assembled Supernanoparticles for Deep-Tissue Bimodal Imaging and Amplified Dual-Mode Heating Treatment. *ACS Nano* **2019**, *13* (1), 408−420.

(32) Xia, Y.; Tang, Z. Monodisperse Inorganic Supraparticles: Formation Mechanism, Properties and Applications. *Chem. Commun.* **2012**, *48* (51), 6320.

(33) Piccinini, E.; Pallarola, D.; Battaglini, F.; Azzaroni, O. Self-Limited Self-Assembly of Nanoparticles into Supraparticles: Towards Supramolecular Colloidal Materials by Design. *Mol. Syst. Des. Eng.* **2016**, *1* (2), 155−162.

(34) Al Zaki, A.; Joh, D.; Cheng, Z.; De Barros, A. L. B.; Kao, G.; Dorsey, J.; Tsourkas, A. Gold-Loaded Polymeric Micelles for Computed Tomography-Guided Radiation Therapy Treatment and Radiosensitization. *ACS Nano* **2014**, *8* (1), 104−112.

(35) Paterson, S.; Thompson, S. A.; Gracie, J.; Wark, A. W.; de la Rica, R. Self-Assembly of Gold Supraparticles with Crystallographically Aligned and Strongly Coupled Nanoparticle Building Blocks for SERS and Photothermal Therapy. *Chem. Sci.* **2016**, *7* (9), 6232−6237.

(36) Heymann, J. A. W.; Shi, D.; Kim, S.; Bliss, D.; Milne, J. L. S.; Subramaniam, S. 3D Imaging of Mammalian Cells with Ion-Abrasion Scanning Electron Microscopy. *J. Struct. Biol.* **2009**, *166* (1), 1−7.

(37) Drobne, D. 3D Imaging of Cells and Tissues by Focused Ion Beam/Scanning Electron Microscopy (FIB/SEM). In *Nanoimaging*; Sousa, A. A., Kruhlak, M. J., Eds.; Humana Press: Totowa, NJ, 2013; pp 275−292.

https://dx.doi.org/10.1021/acs.langmuir.9b03479
Langmuir 2020, 36, 3912−3923

(38) Zhu, M.; Lanni, E.; Garg, N.; Bier, M. E.; Jin, R. Kinetically Controlled, High-Yield Synthesis of Au25 Clusters. *J. Am. Chem. Soc.* **2008**, *130* (4), 1138−1139.
(39) Guo, G.; Ji, L.; Shen, X.; Wang, B.; Li, H.; Hu, J.; Yang, D.; Dong, A. Self-Assembly of Transition-Metal-Oxide Nanoparticle Supraparticles with Designed Architectures and Their Enhanced Lithium Storage Properties. *J. Mater. Chem. A* **2016**, *4* (41), 16128−16135.
(40) Raposo, G.; Stoorvogel, W. Extracellular Vesicles: Exosomes, Microvesicles, and Friends. *J. Cell Biol.* **2013**, *200* (4), 373.
(41) Lamparski, H. G.; Metha-Damani, A.; Yao, J.-Y.; Patel, S.; Hsu, D.-H.; Ruegg, C.; Le Pecq, J.-B. Production and Characterization of Clinical Grade Exosomes Derived from Dendritic Cells. *J. Immunol. Methods* **2002**, *270* (2), 211−226.
(42) Mulcahy, L. A.; Pink, R. C.; Carter, D. R. F. Routes and Mechanisms of Extracellular Vesicle Uptake. *J. Extracell. Vesicles* **2014**, *3* (1), 24641.
(43) Gopal, S.; Chiappini, C.; Penders, J.; Leonardo, V.; Seong, H.; Rothery, S.; Korchev, Y.; Shevchuk, A.; Stevens, M. M. Porous Silicon Nanoneedles Modulate Endocytosis to Deliver Biological Payloads. *Adv. Mater.* **2019**, *31* (12), 1806788.

https://dx.doi.org/10.1021/acs.langmuir.9b03479
Langmuir 2020, 36, 3912−3923